Reaction pathway of the hydrothermal synthesis of $AgCuO_2$ from *in situ* time-resolved X-ray diffraction

*Hongjun Liu[a], Ola G. Grendal[b], Susanne Linn Skjærvø[b,c], Antoine R. M. Dalod[b,d], Wouter van Beek[e], Abderrahime Sekkat[a], Mari-Ann Einarsrud[b], David Muñoz-Rojas[a,]**

a. Univ. Grenoble Alpes, CNRS, LMGP, F-38000 Grenoble, France;

b. Department of Material Science and Engineering, NTNU Norwegian University of Science and Technology, 7491 Trondheim, Norway;

c. Department of Chemistry and Nanoscience Center, University of Copenhagen, 2100 København Ø, Denmark

d. Present address: poLight ASA, Kongeveien 77, 3188 Horten, Norway.

e. SNBL/ESRF, 38043 Grenoble CEDEX 9, France.

Key words: *in situ* X-ray diffraction, time-resolved, $AgCuO_2$, hydrothermal, growth mechanism.

Abstract

$AgCuO_2$ is an interesting semiconductor oxide with appealing optical and electronic properties. While the oxide has been synthesized in bulk by different approaches, no study on the formation mechanism has been carried out to date. We present an *in situ* time-resolved X-ray diffraction

study of the hydrothermal synthesis of $AgCuO_2$ from AgO and CuO. The effects of reaction pH and temperature on the reaction pathways and products have been studied. While pH is a key parameter for the successful synthesis of $AgCuO_2$, temperature affects mainly the reaction kinetics. A reaction pathway is proposed that involves a series of dissolution-precipitation reactions, mediated by Cu and Ag hydroxy complexes. Finally, we have compared different approaches to obtain the reaction activation energy, which was calculated to be 70.6±5.1 kJ/mol. Nevertheless, our results show that new models need to be developed for the type of reaction presented here.

Introduction

Silver copper mixed oxides are an exciting new family of materials.[1] The first member of the family, $Ag_2Cu_2O_3$ was synthesized by Gomez-Romero's group in 1999.[2] $Ag_2Cu_2O_3$, is iso-structural with paramelaconite and involves a 3D interpenetrating network of Ag-O and Cu-O chains. After the first member, $AgCuO_2$ was obtained by electrochemical oxidation of $Ag_2Cu_2O_3$,[3] ozone oxidation,[4] co-precipitation[5] and by hydrothermal synthesis.[6] $AgCuO_2$ crystallizes in a crednerite-type ($CuMnO_2$, $C2/m$) 2D structure,[7] with copper atoms being surrounded by 4 oxygen atoms, in an edge-sharing square-planar coordination, forming CuO_2 chains along the *b* axis (as presented in the supporting information, Figure S1). Contrarily to the 2-fold linear coordination of Cu^{1+} in crednerite, Ag ions in $AgCuO_2$ are coordinated by 6 oxygen ions with a distorted octahedral coordination due to a higher oxidation state than +1, as clearly observed by XPS.[3,6,8] In addition, X-ray absorption spectroscopy (XAS) studies confirmed the oxidation state of Ag to be higher than +1, while revealing that Cu atoms are also oxidized above +2 and that the charges are delocalized between all the atoms in the structure.[7] These results have also been recently supported by Density Function Theory (DFT) calculations by Carreras *et al.*, in which the high oxidation

states of silver and copper are obtained.[9] In views of these results, $AgCuO_2$ is expected to have very interesting transport properties. Sauvage *et al.*[10] measured a p-type electrical conductivity of $AgCuO_2$, three orders of magnitude higher than for Ag_2CuMnO_4, another member of the family with oxidation states of +1 and +2 for Ag and Cu, respectively, and no charge delocalization.[11] Despite the measurements were made on low density pellets (due to the sintering challenges at high temperature leading to the reduction of Ag cations) a conductivity of 3.2×10^{-1} S/cm was obtained for $AgCuO_2$.[10] The high conductivity of $AgCuO_2$ was later confirmed on micron sized single crystals prepared by hydrothermal synthesis.[6] Along these experimental works, DFT calculations by Feng *et al.*[12] predict a small bandgap of about 1.1 eV. However, the recent work by Carreras *et al.*[9] predicts that $AgCuO_2$ is a three-dimensional conductive metal. Thus, more detailed studies are needed to understand this difference from the different DFT calculations.

To date it has not been possible to find a suitable deposition method to obtain high quality and pure $AgCuO_2$ films to carry out a study of the transport and optical properties, and to be implemented in devices. Apart from the synthesis approaches detailed above, which yielded powders, a recent study on the direct electrodeposition of $AgCuO_2$ was reported by Lu *et al.*[13] However the films were very rough, and no electrical characterization was provided. Reactive sputtering has also been used to deposit Ag-Cu mixed oxide films, but to date no there are no reports on the deposition of phase pure, stoichiometric $AgCuO_2$ thin films by this approach.[14–16]

The hydrothermal method is very appealing for the fabrication of high quality crystalline materials at low temperatures and has been extensively used to fabricate devices based on ZnO nanorod arrays, for example.[17–19] In the case of $AgCuO_2$, a hydrothermal approach using AgO suspended in a basic Cu^{2+} solution was developed to obtain large single crystals for *in situ* transport measurements.[6] AgO contains Ag in the oxidation state of +1 and +3 and thus it is capable of

oxidizing the Cu^{2+} cations in solution to form $AgCuO_2$. No detailed study of the reaction mechanism of the formation of $AgCuO_2$ has been published, but a better knowledge of the reaction mechanism and the effect of the different parameters is necessary to optimize the synthesis and provide guidance for the deposition of $AgCuO_2$ thin films.

In this study, we report an *in situ* time-resolved X-ray diffraction study of the hydrothermal synthesis of $AgCuO_2$ varying the solution pH and reaction temperature. By comparing the phase transitions during reactions at different pH values, different reaction pathways and final products were observed. From these, a reaction pathway based on the formation of intermediate Ag and Cu complexes is proposed. Also, we applied two different models (Johnson-Mehl-Avrami-Kolmogorov (JMAK) and Austin-Rickett (AR)) to study the reaction kinetics. Our results show that the JMAK model is more suited than the AR to fit our experimental data, but better models need to be developed for this type of reactions. An activation energy of around 70.6±5.1 kJ/mol was estimated.

Experimental Section

a. Materials and preparation

To study the reaction mechanism and activation energy, the hydrothermal synthesis of $AgCuO_2$ from AgO and $CuSO_4$ was reproduced following a previously described protocol.[6] To maximize the diffraction peak intensity, a dense slurry (suspension) was prepared by mixing 0.262 g (2.11 mmol) of AgO (99.5 %, Sigma Aldrich) and 0.522 g (2.09 mmol) of $CuSO_4 \cdot 5H_2O$ (99 %, Sigma Aldrich) in 6 mL of deionized water, which was mechanically stirred for 5 min. Based on the pH chosen for the experiment, a given amount of KOH (99 %, Sigma Aldrich) (giving 0, 0.3 and 1 M)

was added to the suspension, which was mixed for a further 5 min. To facilitate the injection into the reaction cell, the slurry was first mildly ground using an agate mortar. Due to the difficulty of recovering the reaction product from the capillary after the *in situ* experiments, parallel syntheses were conducted in a conventional approach to be able to characterize the reaction products *ex situ* and to perform pH measurement before and after the hydrothermal treatment. These experiments were performed by mixing 0.524 g (4.22 mmol) AgO and 1.044 g (4.18 mmol) of $CuSO_4 \cdot 5H_2O$ in 12 mL deionized water followed by the addition of 0.68 g (12 mmol), 0.20 g (3.6 mmol) or 0 g of KOH to have the different pH tested *in situ* (1, 0.3 and 0 M KOH, respectively). The reactions were performed in Pyrex (25 ml) bottles (that were maintained in the dark) at different temperatures from 50 to 120 °C for 10 h. Table S1 in the SI summarizes the pH values and the color of the solution and the resulting powders for the different reactions.

b. Characterization

The *in situ* X-ray diffraction (XRD) experiments were conducted at the Swiss-Norwegian Beamlines (BM01) at the European Synchrotron Radiation Facilities (ESRF), Grenoble, France (Table 1). The experiments were performed in transmission mode using the PILATUS@SNBL platform with a wavelength $\lambda = 0.6999$ Å.[20] The reaction cell has been described in detail in previous works,[21–23] and is shown in Figure 1. A single crystal sapphire capillary serves as a miniature reaction cell, with 1.15 ± 0.1 mm outer and 0.8 ± 0.08 mm inner diameters. The slurries were injected into the reaction cell with a plastic syringe. Once the capillary was filled with slurry, one end was closed and the other end was connected to a HPLC pump (high-pressure liquid chromatography pump, Shimadzu LC-10ADVP, Shimadzu Corporation).

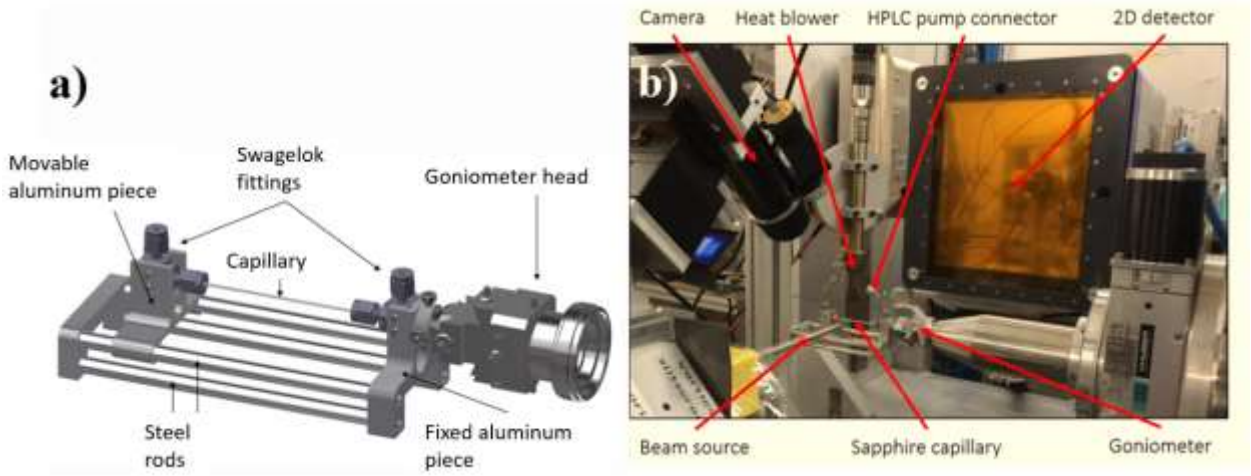

Figure 1. a). 3D Scheme of the capillary *in situ* cell used (drawn with Autodesk(R) Inventor LTTM by Anders Bank Blichfeld). [22] b). *In situ* XRD experimental setup at line BM01A, ESRF, including X-ray source, 2D detector, heater, capillary cell, goniometer and CCD camera.

Table 1. Overview of in situ XRD measurements performed including the different parameters used during the hydrothermal synthesis and the phases obtained. S1-S3 were prepared varying the KOH concentration while the T1-T5 samples were synthesized at different temperatures.

Sample name	**Temperature (°C)**	**KOH solution concentration**	**Main Obtained phase (weight fraction in parenthesis, secondary phases in italics)**	**Estimated completion time (s)**
S1	90	1	$AgCuO_2$ (83) *CuO (8), Ag_2O (9)*	N/A
S2		0.3	$Cu_4(SO_4)(OH)_6$ *(AgO, Ag)*	
S3		0	$Cu_4(SO_4)(OH)_6$ (with intermediate phases)	
T1	50	1	$AgCuO_2$ (83) *CuO (11), Ag_2O (6)*	3980
T2	70		$AgCuO_2$ (83) *AgO (4) CuO (8), Ag_2O (5)*	864
T3	80		$AgCuO_2$ (92) *CuO (7), Ag_2O (1)*	297
T4 (=S1)	90		$AgCuO_2$ (83) CuO (8), Ag_2O (9)	286

T5	120		$AgCuO_2$ (92) CuO (5), Ag_2O (2)	52

A pressure of 250 bar was applied to avoid boiling during the reaction. In order to evaluate a possible effect of pressure, experiment S1 was also performed without applying pressure and no significant effect of pressure on the final composition or refined parameters was observed. A high temperature heat blower (Leister LE Mini 800) with N_2 gas flow was used for heating. Acquisition times were optimized for the different reaction rates, 5 s for the fastest reactions and 10 s for the slower reactions. In order to eliminate the possibility of having light-induced reactions (Ag compounds being photosensitive), the whole reaction and characterization process was carried out in the dark. Parasitic regions (spots from sapphire capillary and shadow from beam stopper) were masked from the raw data using the Bubble software, as described in previous works.[20]

The masked 2D data were integrated into 1D also using the Bubble software. Temperature calibrations were performed with boron nitride powder[24] inside a sapphire capillary. The instrumental broadening was calibrated with a NIST 660a LaB_6 standard.[21,25] All suspensions were prepared right before the diffraction experiments (no more than 10 minutes). The morphology characterization of the product from the parallel syntheses conducted in Pyrex bottles were carried out using a SEM-FEG Environmental FEI QUANTA 250 Scanning Electron Microscope (SEM).

c. Parameter refinement

Rietveld refinements were performed using Topas v. 5 to fit a model to the XRD patterns for experiments conducted at 50, 80 and 120 °C. Strain and unit cell parameters of Ag_2O were refined from the last frame and these values were kept fixed. Then, the same was conducted for CuO and AgO from the first frame (this was performed individually for all experiments). All these

parameters were kept fixed during the batch Rietveld refinements, which was necessary for maintaining the stability of the refinements, since several of the reflections were overlapping (see supplementary information for details). For the batch Rietveld refinement, scale factor, unit cell parameters (*a, b, c* and *β*), strain and thermal parameters for Ag and Cu in $AgCuO_2$ phase were refined for all frames.

Results and discussion

For reaction S1, in which 1 M KOH was used, $AgCuO_2$ was obtained, as expected. In Figure 2a, several representative XRD patterns have been selected and plotted and aligned with reference patterns. The 2D evolution of the diffraction patterns versus reaction time (y axis) is presented in Figure 2b (the corresponding 3D phase evolution plot is presented in Figure S2a in the SI). From the 2D diagram, variations of the intensity of the different reflections consistent with the formation of $AgCuO_2$ at the expenses of CuO and AgO were observed. Figure S3 in the SI shows the evolution with time of the weight fraction of the different phases as extracted from the refinements for the reactions performed at 50, 80 and 120 °C. The line emerging at low angle (about 7°) shows the formation of the $AgCuO_2$ phase, along with several other reflections at 14.0°, 14.5°, 18.4°. The starting precursors of the reaction were AgO and freshly precipitated CuO (obtained from the precipitation of $CuSO_4$ in the 1 M KOH solution), giving the two diffraction lines at 15.9° and 17.4°, respectively, which decrease rapidly. Meanwhile, traces of Ag_2O from AgO reduction were also observed at a diffraction angle of 14.5°. This is likely due to the thermal decomposition of AgO in the reaction process, before oxidized Ag cations became stabilized in the $AgCuO_2$ structure. With a high solubility in water, the reflections of other species, like KOH or K_2SO_4 were not present in the diffraction patterns, but contribute to the background signal, which is sensibly higher than for powder samples (Figure S2a).

The results for the hydrothermal reaction with a lower KOH concentration (0.3 M, sample S2) are shown in Figures 2c (representative XRD patterns with reference patterns) and 2d (2D evolution of the diffraction patterns, the corresponding 3D plot is shown in Figure S2b). In this case, $AgCuO_2$ was not obtained. At low diffraction angles, two emerging reflections were observed corresponding to the final $Cu_4(SO)_4(OH)_6$ phase. Similar to sample S1, a continuous evolution with no intermediate phases was observed. From the diffraction pattern, an increase of the background signal was presented between 10° and 20°, which can be correlated to the higher concentration of dissolved silver ions, [26] since the Ag-containing phases were barely seen in the final product (unreacted AgO and metallic Ag, both in small amounts). The precipitation of the basic copper sulfate results in an acidification of the solution (Table S1 presents the initial pH values of the solutions for the different reactions), with a concomitant dissolution of the AgO, as evidenced by the decrease of the intensity of the reflection at 14.5°.

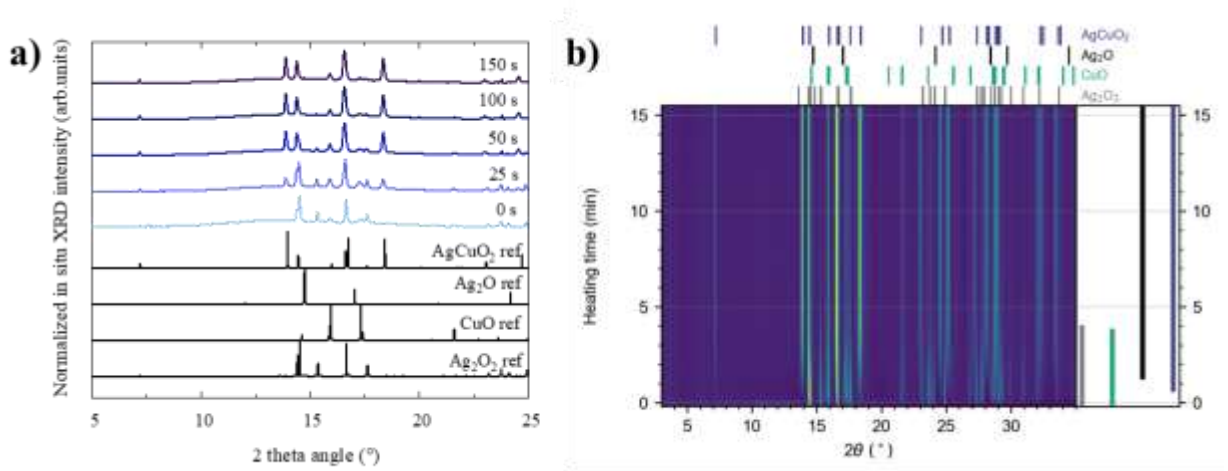

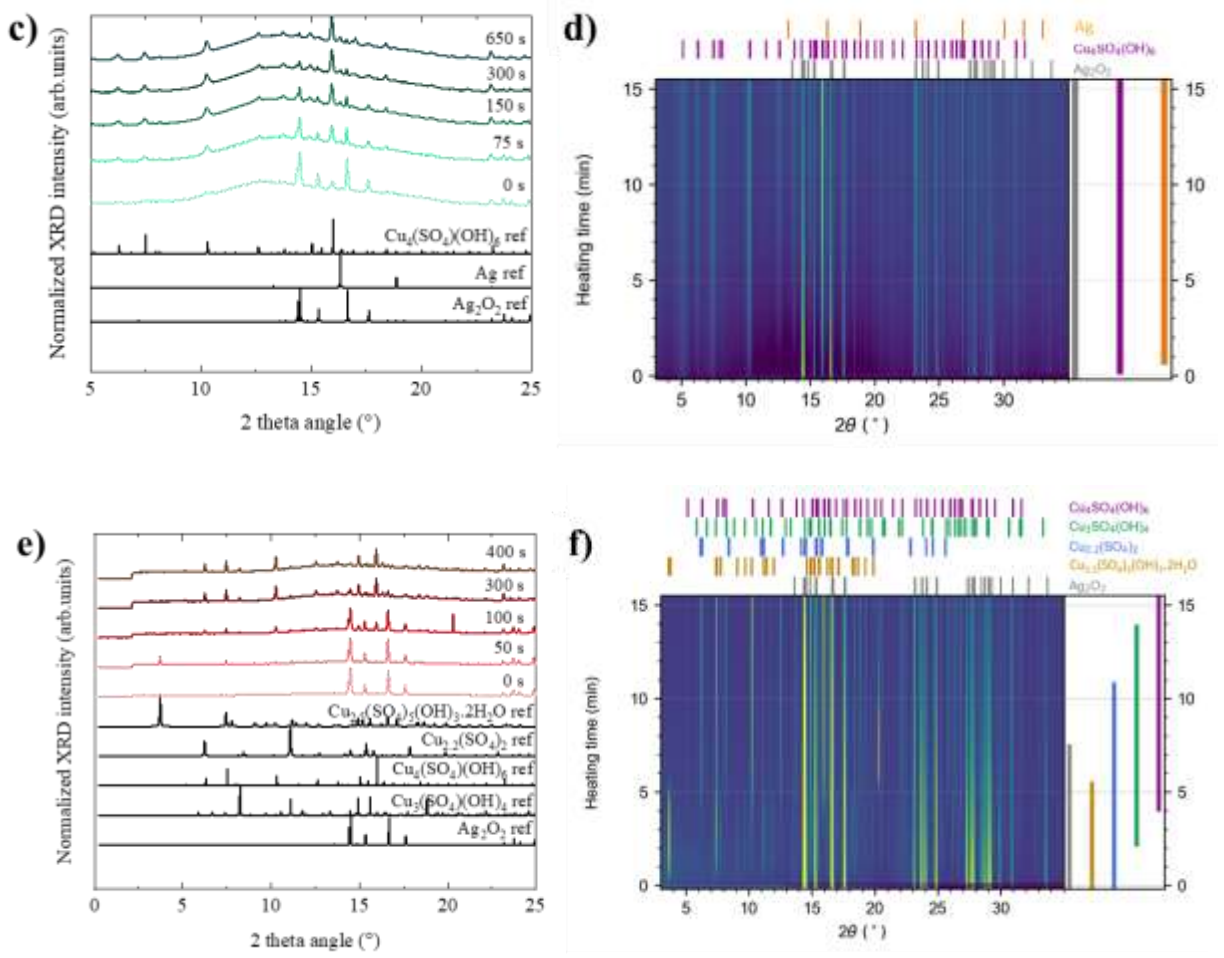

Figure 2. a) representative XRD patterns during reaction S1 and b) phase evolution, with 1 M KOH solution at 250 bar and 90 °C; c) representative XRD patterns during reaction S2 and d) phase evolution, with 0.3 M KOH at 250 bar and 90 °C; e) representative XRD patterns during reaction S3 and phase evolution, with no KOH at 250 bar and 90 °C.

Lastly, in the case of the reaction without KOH added (sample S3), the results are shown in Figure 2e (representative XRD patterns with reference patterns) and 2f (2D evolution of the diffraction patterns, the corresponding 3D plot is shown in Figure S2c). The phase evolution map presented in this case shows a rather different scenario. At low diffraction angles, a reflection emerged right after the start of the experiment and it disappeared after about 100 s. Several diffraction lines were

observed during the reaction, showing the existence of intermediate phases. Similar evidence of intermediate phases can also be evidenced by the reflection at around 23°. Comparing to the reference patterns, the emergence and disappearance of these reflections were actually caused by a phase transition from $Cu_{2.5}(SO_4)_5(OH)_3 \cdot 2H_2O$ to $Cu_3(SO_4)(OH)_4$ and finally stabilized as the $Cu_4(SO_4)(OH)_6$ phase. Meanwhile, the reflections corresponding to AgO totally disappeared after about 10 min of reaction. This is again caused by the acidification of the suspension as the basic copper sulfate phases precipitate and transform (see table S1 in SI). Indeed, the formation of different types of copper sulfate hydroxide phases was reported in a work by Tanaka *et al.*[27] In their work, a $CuSO_4$ solution (1 M) was titrated against a NaOH solution (0.01 M, pH 12). As different quantities of $CuSO_4$ solution were added, different copper sulfate hydroxide phases were formed. Initially, $Cu(OH)_2$ was obtained as expected, and then other basic copper sulfates formed. For instance, $Cu_4(SO_4)(OH)_6$ formed when the solution had neutral pH and even at pH as low as 4 after further additions of $CuSO_4$ solution. Reactions carried out with only AgO as starting precursor, in both 0 and 1 M KOH solutions did, on the other hand, not result in any observable reaction or dissolution, AgO being the only phase detectable by XRD after the hydrothermal reaction, as indicated in Table S1.

Hence, the pH of the solution plays a critical role in $AgCuO_2$ formation. Different pH values during the reaction led to different reaction schemes between $CuSO_4$ and AgO, resulting in different final products. The fact that $AgCuO_2$ is only obtained when high pH values are used, would imply that the reaction proceeds via the formation of soluble Cu and Ag basic species that then would coprecipitate. For Cu, it is known that it can form soluble hydroxide complexes in basic solutions. For Ag, the formation of such complexes has also been described in the past,[28] and the sulfate ions could also play a role in the formation of soluble complexes.[29]

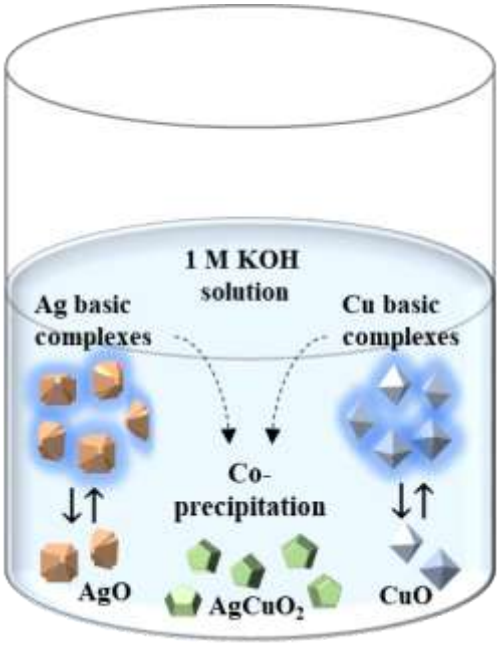

Figure 3. Illustration of the proposed $AgCuO_2$ phase formation pathway at high pH facilitating the co-precipitation.

Combining the results obtained from the different reactions discussed so far, we propose a reaction pathway for the hydrothermal synthesis of $AgCuO_2$, as illustrated in Figure 3. At the beginning of the reaction, the dissolution of $CuSO_4$ in the 1 M KOH solution induces the precipitation of CuO,[30] as confirmed by the reflections at the beginning of the reaction (Figure 2b). Therefore, the actual reaction precursors in 1 M KOH solution are CuO and AgO. In this starting slurry, there is always an equilibrium between the metal oxide and the metal hydroxide complex, as shown in Equations 1 and 2.[28] In the case of AgO, the solubility of such complexes is rather low (in the range of 10^{-14} mol/L).[28,31]

$$AgO + xOH^- \rightleftarrows [Ag(OH)_x]_{aq}^{2-x} \quad \textbf{(1)}$$

$$CuO + xOH^- \rightleftarrows [Cu(OH)_x]_{aq}^{2-x} \quad \textbf{(2)}$$

$$[Ag(OH)_x]_{aq}^{2-x} + [Cu(OH)_x]_{aq}^{2-x} \rightarrow AgCuO_2 \downarrow + 2H_2O + (2x-4)OH^- \quad \textbf{(3)}$$

Then, $AgCuO_2$ forms as a result of a co-precipitation between $[Ag(OH)_x]^{2-x}$ and $[Cu(OH)_x]^{2-x}$, as shown in Equation 3. It should be noted that we are dealing with diffraction data only, so the possibility of having mixed metal complexes or an amorphous precursor of $AgCuO_2$ rapidly crystallizing to the final crystalline sample, cannot be excluded. The fact that $AgCuO_2$ forms at high pH conditions implies that it is much less soluble than AgO or CuO in basic solutions.[13,32] Therefore, the silver and copper hydroxide complexes in solution are consumed by $AgCuO_2$ precipitation, displacing the equilibrium between the metal oxides and metal hydroxide complex towards the latter.

In addition to studying the effects of pH on the reaction outcome and pathway, the effects of reaction temperature were also investigated. The KOH concentration was maintained at 1 M with 250 bar pressure and the reaction temperature was varied from 50 to 120 °C, as shown in Table 1. Since the initial suspension used had the same concentration in all cases, the quantity of injected reactants in the capillary is assumed to be the same. For all the reaction temperatures, $AgCuO_2$ was obtained as the final product and similar reaction evolution was observed, with the intensity of XRD reflections corresponding to AgO and CuO decreasing while the reflections for $AgCuO_2$ increased in intensity (The evolution with time of the weight fraction of the different phases for different temperatures, as extracted from the refinements, is plotted in Figure S3). Meanwhile, weak X-ray reflections of Ag_2O were also observed, which could be due to the thermal decomposition of AgO, as stated above. Conversely, metallic Ag was never detected in the XRD patterns.

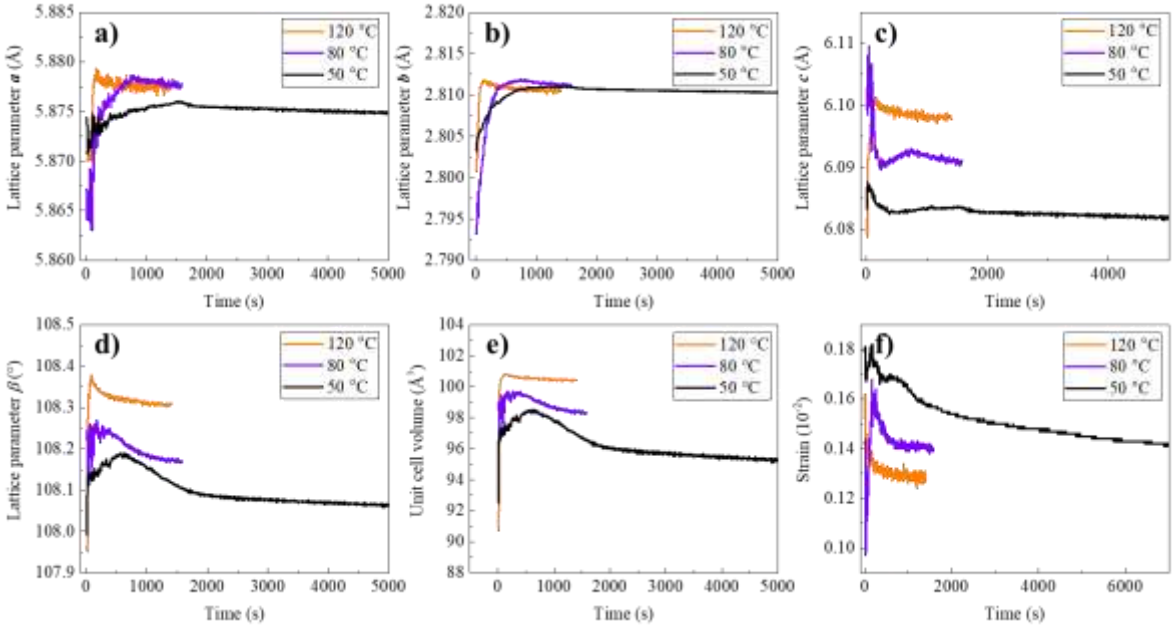

Figure 4. Time resolved refined values for $AgCuO_2$. a), b), c) and d) unit cell parameters (lattice parameters *a*, *b*, *c* and *β*), e) unit cell volume and f) strain.

The evolution of the lattice parameters, unit cell volume and micro strain for the $AgCuO_2$ crystals varied differently with regard to the reaction time and temperature, as presented in Figure 4 (the refinement of crystallite size was also performed but no reliable values could be obtained). In Figure 4a, 4b and 4c, the unit cell parameters *a, b, c* generally exhibited a rapid increase once the reaction started, before decreasing to smaller final values. For cell parameter *a*, at 120 °C, the value reached a maximum almost instantly after the reaction was initiated, and stabilized at about 5.878 Å. Meanwhile at the lower reaction temperatures of 80 and 50 °C, the increase was less drastic and a reached a maximum followed by a slight decrease. The value of *a* stabilized around 5.873 Å at 50 °C. This variation of the parameter *a* (value increase and then decrease) could be related to the re-organization of the lattice. It has to be taken into account that the $AgCuO_2$ formation takes place even at room temperature[6] and thus we expect small amounts of $AgCuO_2$ to

be present from the first XRD pattern acquired. A similar evolution was observed for parameter *b* (Figure 4b), and similar values are obtained at 120 and 50 °C. Conversely, a clear difference of about 0.015 Å was observed for the *c* parameter: 6.098 Å at 120 °C and 6.083 Å at 50 °C (Figure 4c). The *c* parameter showed more variation as the reaction proceeded, compared to parameters *a* and *b*. Figure 4d shows the variation in β and the difference at the highest and lowest reaction temperature was about 0.25°. As stated above the different evolution and final values of the cell parameters at different temperatures could be due to lattice rearrangements. Parameter *b* lies parallel to the CuO_2 chains in which Cu atoms are coordinated by 4 oxygen atoms (with edge-sharing square-planar coordination), and to the chains of Ag octahedra. The similar final values of parameter *b* for the different reaction temperatures are thus rather logical. Contrarily, twisting of the CuO_2 chains or any other lattice rearrangement is more likely to take place in the *ac* plane, which again agrees with the evolution and different final values observed for parameters *a* and *c*.

The unit cell volume presented in Figure 4e increased after the initiation of the reaction followed by a decrease to a lower final value (i.e. following the evolution observed for the cell parameters). Larger unit cells are observed for reactions at higher temperature, 100.8 $Å^3$ at 120 °C and 95.8 $Å^3$ at 50 °C, as expected from the thermal expansion of the lattice. As in previous studies, the values are nevertheless higher than what would be expected for a solid sample, but the presence of hydroxyl ions or water molecules within the structure has been proposed to account for it.[25,33,34] Lastly, the strain was also monitored for the different temperatures (Figure 4f). For crystals formed at higher temperatures, the strains were generally lower than those formed at lower temperatures, again as expected since higher temperatures are favoring a better crystallization and strain relaxation. At 120 °C, about 0.00128±0.00003 of strain was observed and about 0.00143±0.00002 for 50 °C, in agreement with the diffraction reflection width observed in Figure 4a, 4b and 4c.

In addition to the unit cell parameters, the atomic thermal displacement factor (B_{iso}) of Ag and Cu atoms in the $AgCuO_2$ crystals were refined for the different temperatures and results are shown in Figure 5. For Ag, the B_{iso} value decreased rapidly once the reaction was initiated (Figure 5a). Conversely, for Cu there was a rapid initial decrease followed by an increase of the B_{iso} values (Figure 5b). The B_{iso} values obtained are rather large, which is similar to what we have observed in previous *in situ* studies.[33] Again, the presence of hydroxyl groups could be the reason for the higher B_{iso} values obtained in these type of studies.[34]

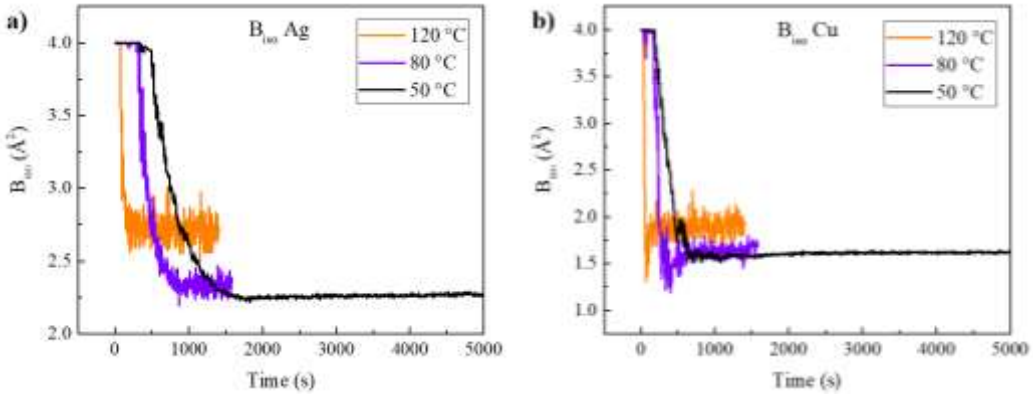

Figure 5. B_{iso} values for Ag a) and Cu b) in $AgCuO_2$ as a function of time.

For $AgCuO_2$ crystals formed at all the reaction temperatures, the Ag atom B_{iso} values are generally larger than those for Cu atoms, indicating a higher thermal motion for Ag ions in the $AgCuO_2$ crystals. In any case, the high B_{iso} values obtained for $AgCuO_2$ are in agreement with previous XAS data, and are the result of the peculiar electronic structure of this oxide, with intermediate oxidation states and charge delocalization.[7] In particular, Ag B_{iso} values are always larger than for Cu, which could be related to the high mobility of silver anions, as for example in AgI, where Ag ions are mobile inside the fixed lattice of I^- anions.[35] This is in agreement with the recent DFT

calculations by Carreras *et al*., which predict an easy slide of Ag atoms along the chains of linearly coordinated Ag cations.[9]

To estimate the activation energy for the hydrothermal formation of $AgCuO_2$ from AgO and CuO in a basic solution, two models were compared, namely, the Johnson-Mehl-Avrami-Kolmogorov (JMAK) model and the Austin-Rickett (AR) model. In these models the extent of reaction, f, is described, respectively, by Equations 9 and 10.

$$\boldsymbol{f = 1 - \exp(-k(t - t_0)^n)} \quad \textbf{(1)}$$

$$\boldsymbol{f = 1 - (k(t - t_0)^n + 1)^{-1}} \quad \textbf{(10)}$$

$\boldsymbol{k}$ is the reaction rate constant, t is the time after t_0 of appearance of the phase, and $\boldsymbol{n}$ is linked to the growth mechanism. Both models have been used to interpret precipitation and phase-change reactions.[36,37] The normalized fitting results are shown in Figure S4 and the fitted results of $\boldsymbol{n}$, $\boldsymbol{k}$ values are presented in Table 2.

Table 2. Fitted $\boldsymbol{n}$ and $\boldsymbol{k}$ values from JMAK and AR models.

Temperature (K)	k_j **(JMAK fitted reaction rate constant)**	n_j **(JMAK fitted)**	k_a **(AR fitted reaction rate constant)**	n_a **(AR fitted)**
323	0.0359±0.0002	1.94±0.03	0.0451±0.0006	2.84±0.11
343	0.1329±0.001	1.78±0.02	0.1697±0.0020	2.62±0.09
353	0.4813±0.0023	1.95±0.03	0.6015±0.008	2.95±0.11
363	0.6568±0.0036	1.95±0.03	0.8192±0.008	2.92±0.08

393	3.6605±0.1629	1.90±0.03	4.5830±0.1368	3.87±0.21

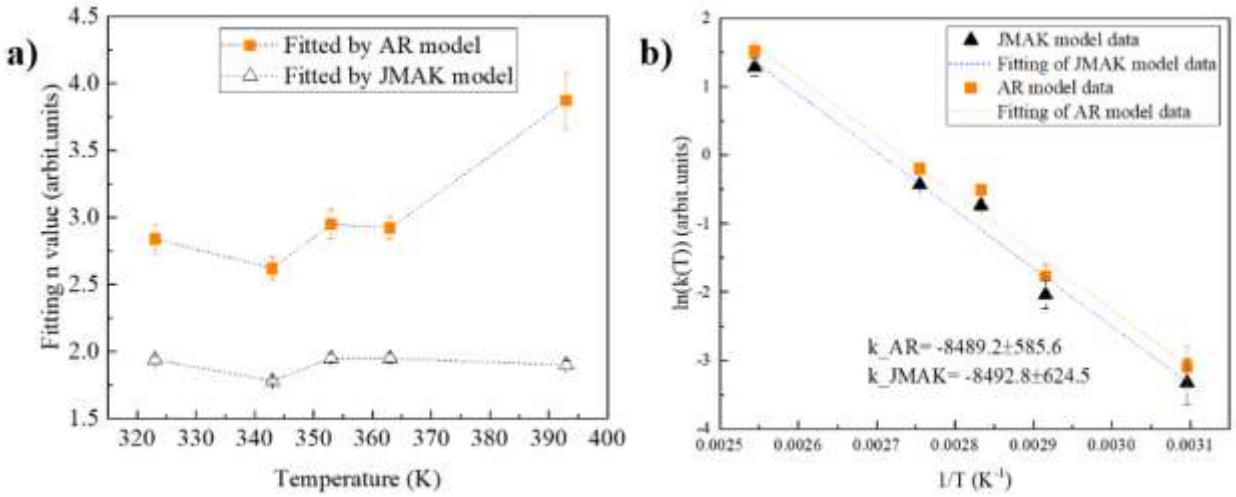

Figure 6. a) Fitted n values from both JMAK and AR models. b) Activation energy estimated from both JMAK and AR models, Ea_JMAK = 70.6±5.2 kJ/mol and Ea_AR = 70.6±4.9 kJ/mol, k_AR and k_JMAK in figure are the fitted slopes.

To evaluate the reaction durations at a range of temperatures, we set 90 % as the indication of an accomplished reaction. As observed from the fittings, the obtained k(T) (fitted line slope) using both models are rather similar, showing an exponential increase with temperature. However, the ***n*** values deduced from the different fitting models exhibit a clear difference, as shown in Table 2 and Figure 6a. From the AR model, the ***n*** values obtained increased from 2.7 to almost 3.8 with increasing reaction temperature. Meanwhile, from the JMAK model the fittings are rather reasonable for all reactions, ***n*** values around 2 being obtained. A comparison of both models (Figure S4) shows that the JMAK model fits better than the AR model in our case. The obtained ***n*** values around 2 would indicate that the growth is restricted to 1 or 2 dimensions, according to the litterature.[38–40] This would imply that in all cases the particles obtained would have similar shapes, but SEM images of the different products obtained from hydrothermal reactions performed

sealed Pyrex bottles (see experimental details) show two different type of particles at low and high temperatures (Figure 7). The $AgCuO_2$ particles tend to be bi-dimensional with a platelet-type shape for reaction temperatures from 50 to 80 °C. Conversely, for 90 and 120 °C, the particles are more spherical (see figure S5 in the SI for lower magnification images). Thus, it seems clear that none of the two models can fully explain the reaction taking place in this case, especially as reaction temperature decreases, as evidenced by the worse fittings obtained (figure S4). More studies and new models are therefore needed. In particular, it has been shown that when dealing with nanomaterials, particle growth via the oriented attachment mechanism (as opposed to the classical Ostwald ripening model) often plays a key role at hydrothermal conditions.[41,42] The development of new kinetic models taking oriented attachment into account have been tackled, requires an exhaustive HRTEM study of the samples.[43] The different kinetics and particle shape of the samples obtained at different temperatures could in fact be due to oriented attachment taking place at lower temperatures, but a deeper study should be performed to evaluate this hypothesis.

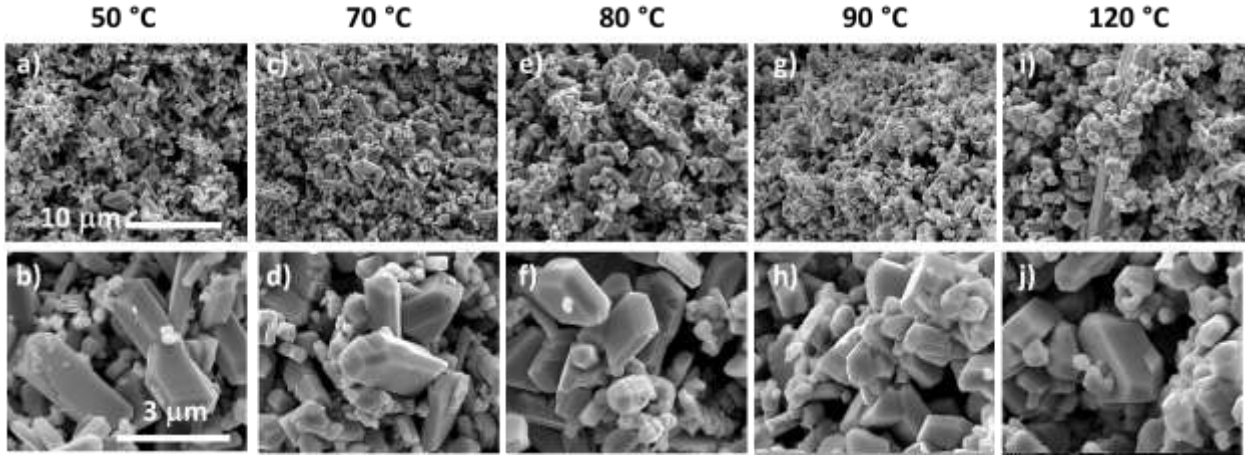

Figure 7. SEM images of $AgCuO_2$ powders synthesized in 1 M KOH solution in sealed Pyrex bottles for 16 h at 50 °C (a,b), 70 °C (c,d), 80 °C (e,f), 90 °C (g,h) and 120 °C (i,j). The scale bar for images a to i is 10 microns, and 3 microns for images b to j.

From our fittings (Figure 6b), the activation energies for the whole reaction obtained from the two models are rather similar, at 70.6 kJ/mol. Given the limited applicability of these models for our cases, as discussed above, this value needs to be taken as approximated. In our case, $AgCuO_2$ forms at room temperature and is detectable at the beginning of the experiments even before heating, thus meaning that both the dissolution of initial oxides and the precipitation of $AgCuO_2$ can take place at room temperature. With this in mind, and given that the activation energy obtained for the reaction is comparable to other similar precipitation reactions,[44,45] we propose that it corresponds to the nucleation of $AgCuO_2$ from the complexes.

Conclusions

In this work, we present an *in situ* time-resolved XRD study of the reaction mechanism of the hydrothermal synthesis of $AgCuO_2$ evaluating the effect of both solution pH and reaction temperature. By varying the solution pH, different reaction intermediates and final products were formed, and $AgCuO_2$ could only be obtained when using 1 M KOH solutions in this work. Based on our analyses, we have proposed a reaction pathway that is based on the co-precipitation of silver and copper hydroxide complexes in alkaline solution. The cell parameters increased when increasing the reaction temperature and the *c* and *b* parameters were the most sensitive to the temperature. Relatively high B_{iso} values comparable to similar studies were observed. In all cases, the B_{iso} values for Ag where higher than for Cu. This is believed to be due to the intrinsic high mobility of Ag atoms, which could be favored in $AgCuO_2$ given the peculiar electronic structure and 6-fold coordination of the Ag atoms. Finally, we compared the JMAK and AR models for the calculation of the ***n*** values and the activation energy. Although in our case the JMAK model

provides a better fitting of the data, the ***n*** values obtained do not match the morphology of the particles obtained and thus better models need to be developed. An approximative activation energy of 70.6±5.1 kJ/mol was obtained, which we propose corresponds mainly to the nucleation of the $AgCuO_2$ phase. The insight gained on the formation pathway of $AgCuO_2$ should allow an optimization of the conditions to obtain high quality, dense $AgCuO_2$ films. For example, $AgCuO_2$ nuclei obtained from reactions carried out at low temperature could be deposited on a substrate to then grow a film by performing the electrodeposition or hydrothermal reaction at higher temperatures.

Supporting Information

Crystal structure of $AgCuO_2$ (Figure S1), 3D phase evolution of reaction S1(Figure S2), pH and solution color before and after the hydrothermal reactions (Table S1), evolution with time of the weight fraction of the different phases (Figure S3), comparison of fitting by JMAK and AR models (Figure S4), and SEM images of $AgCuO_2$ powders (Figure S5).

Acknowledgements

HL acknowledges the Ministère de l'Education nationale, de l'Enseignement supérieur et de la Recherche in France for a Ph.D. grant. We acknowledge SNBL at ESRF, Grenoble, France for the granted beam time. DMR acknowledges funding through the Marie Curie Actions (FP7/2007-2013, Grant Agreement No. 631111). Financial support from NTNU Norwegian University of Science and Technology and The Research Council of Norway under the Toppforsk program to the project (No 250403) “From Aqueous Solutions to oxide Thin films and hierarchical Structures” is gratefully acknowledged.

References

(1) Muñoz-Rojas, D. Silver-Copper Mixed Oxides. *Mater. Today* **2011**, *14*, 119–119.

(2) P. Gomez-Romero, E. M. Tejada-Rosales, M. R. P. $Ag_2Cu_2O_3$: The First Silver Copper Oxide. *Angew. Chem. Int. Ed.* **1999**, *38*, 524–525.

(3) Muñoz-Rojas, D.; Oró, J.; Gómez-Romero, P.; Fraxedas, J.; Casañ-Pastor, N. Electrochemically Induced Reversible Solid State Transformations: Electrosynthesis of $Ag_2Cu_2O_4$ by Room Temperature Oxidation of $Ag_2Cu_2O_3$. *Electrochem. commun.* **2002**, *4*, 684–689.

(4) Muñoz-Rojas, D.; Fraxedas, J.; Gómez-Romero, P.; Casañ-Pastor, N. Room Temperature Solid-State Transformation from $Ag_2Cu_2O_3$ to $Ag_2Cu_2O_4$ by Ozone Oxidation. *J. Solid State Chem.* **2005**, *178*, 295–305.

(5) Curda, J.; Klein, W.; Jansen, M. $AgCuO_2$—Synthesis, Crystal Structure, and Structural Relationships with CuO and $AgIAgIIIO_2$. *J. Solid State Chem.* **2001**, *162*, 220–224.

(6) Muñoz-Rojas, D.; Córdoba, R.; Fernández-Pacheco, A.; De Teresa, J. M.; Sauthier, G.; Fraxedas, J.; Walton, R. I.; Casañ-Pastor, N. High Conductivity in Hydrothermally Grown $AgCuO_2$ Single Crystals Verified Using Focused-Ion-Beam-Deposited Nanocontacts. *Inorg. Chem.* **2010**, *49*, 10977–10983.

(7) Muñoz-Rojas, D.; Subias, G.; Fraxedas, J.; Gomez-Romero, P.; Casan-Pastor, N. Electronic Structure of $Ag_2Cu_2O_4$. Evidence of Oxidized Silver and Copper and Internal Charge Delocalization. *J. Phys. Chem. B* **2005**, *36*, 6193–6203.

(8) Muñoz-Rojas, D.; Fraxedas, J.; Oró, J.; Gómez-Romero, P.; Casañ-Pastor, N. Structural Study of Electrochemically-Synthesized $Ag_2Cu_2O_4$. A Novel Oxide Sensitive to Irradiation. *Cryst. Eng.* **2002**, *5*, 459–467.

(9) Carreras, A.; Conejeros, S.; Camón, A.; García, A.; Casañ-Pastor, N.; Alemany, P.; Canadell, E. Charge Delocalization, Oxidation States, and Silver Mobility in the Mixed Silver–Copper Oxide $AgCuO_2$. *Inorg. Chem.* **2019**, *58*, 7026-7035.

(10) Sauvage, F.; Muñoz-Rojas, D.; Poeppelmeier, K. R.; Casañ-Pastor, N. Transport Properties and Lithium Insertion Study in the P-Type Semi-Conductors $AgCuO_2$ and $AgCu_{0.5}Mn_{0.5}O_2$. *J. Solid State Chem.* **2009**, *182*, 374–380.

(11) Muñoz-Rojas, D.; Subías, G.; Oró-Solé, J.; Fraxedas, J.; Martínez, B.; Casas-Cabanas, M.; Canales-Vázquez, J.; González-Calbet, J.; García-González, E.; Walton, R. I.; Casañ-Pastor, N. Ag_2CuMnO_4: A New Silver Copper Oxide with Delafossite Structure. *J. Solid State Chem.* **2006**, *179*, 3883–3892.

(12) Feng, J.; Xiao, B.; Chen, J. C.; Zhou, C. T.; Du, Y. P.; Zhou, R. Optical Properties of New Photovoltaic Materials: $AgCuO_2$ and $Ag_2Cu_2O_3$. *Solid State Commun.* **2009**, *149*, 1569–1573.

(13) Lu, Q.; Lu, K.; Zhang, L.; Gong, J.; Liu, R. Electrodeposition of $AgCuO_2$ Nanoplates. *J. Electrochem. Soc.* **2017**, *164*, D130–D134.

(14) Pierson, J. F.; Rolin, E.; Clément-Gendarme, C.; Petitjean, C.; Horwat, D. Effect of the Oxygen Flow Rate on the Structure and the Properties of Ag-Cu-O Sputtered Films Deposited Using a Ag/Cu Target with Eutectic Composition. *Appl. Surf. Sci.* **2008**, *254*,

6590–6594.

(15) Hari Prasad Reddy, M.; Sreedhar, A.; Uthanna, S. Structural, Surface Morphological and Optical Properties of Nanocrystalline Cu_2O Films Prepared by RF Magnetron Sputtering: Substrate Bias Effect. *Indian J. Phys.* **2012**, *86*, 291–295.

(16) Reddy, Mh. P.; Reddy, P. N.; Sreedhar, B.; Pierson, J. F.; Uthanna, S. Effect of Substrate Temperature on the Structural, Electrical and Optical Behaviour of Reactively Sputtered Ag – Cu – O Films. *Phys. Scr.* **2011**, *84*, 045602.

(17) Parize, R.; Katerski, A.; Gromyko, I.; Rapenne, L.; Roussel, H.; Kärber, E.; Appert, E.; Krunks, M.; Consonni, V. $ZnO/TiO_2/Sb_2S_3$ Core-Shell Nanowire Heterostructure for Extremely Thin Absorber Solar Cells. *J. Phys. Chem. C* **2017**, *121*, 9672–9680.

(18) Yoo, I.-H.; Kalanur, S. S.; Lee, S. Y.; Eom, K.; Jeon, H.; Seo, H. Uniform ZnO Nanorod/Cu $_2$ O Core–Shell Structured Solar Cells by Bottom-up RF Magnetron Sputtering. *RSC Adv.* **2016**, *6*, 82900–82906.

(19) Cossuet, T.; Appert, E.; Thomassin, J.-L.; Consonni, V. Polarity-Dependent Growth Rates of Selective Area Grown ZnO Nanorods by Chemical Bath Deposition. *Langmuir* **2017**, *33*, 6269-6279.

(20) Dyadkin, V.; Pattison, P.; Dmitriev, V.; Chernyshov, D. A New Multipurpose Diffractometer PILATUS@SNBL. *J. Synchrotron Radiat.* **2016**, *23*, 825–829.

(21) Skjaervø, S. L.; Sommer, S.; Nørby, P.; Bøjesen, E. D.; Grande, T.; Iversen, B. B.; Einarsrud, M.-A. Formation Mechanism and Growth of $MNbO_3$, M=K, Na by in Situ X-

Ray Diffraction. *J. Am. Ceram. Soc.* **2017**, 1–8.

(22) Jensen, K. M. Ø.; Christensen, M.; Juhas, P.; Tyrsted, C.; Bøjesen, E. D.; Lock, N.; Billinge, S. J. L.; Iversen, B. B. Revealing the Mechanisms behind SnO_2 Nanoparticle Formation and Growth during Hydrothermal Synthesis: An in Situ Total Scattering Study. *J. Am. Chem. Soc.* **2012**, *134*, 6785–6792.

(23) Becker, J.; Bremholm, M.; Tyrsted, C.; Pauw, B.; Jensen, K. M. O.; Eltzholt, J.; Christensen, M.; Iversen, B. B. Experimental Setup for in Situ X-Ray SAXS/WAXS/PDF Studies of the Formation and Growth of Nanoparticles in near-and Supercritical Fluids. *J. Appl. Crystallogr.* **2010**, *43*, 729–736.

(24) Pease, R. S. An X-Ray Study of Boron Nitride. *Acta Crystallogr.* **1952**, *5*, 356–361.

(25) Dalod, A. R. M.; Grendal, O. G.; Skjærvø, S. L.; Inzani, K.; Selbach, S. M.; Henriksen, L.; Van Beek, W.; Grande, T.; Einarsrud, M. A. Controlling Oriented Attachment and in Situ Functionalization of TiO_2 Nanoparticles during Hydrothermal Synthesis with APTES. *J. Phys. Chem. C* **2017**, *121*, 11897–11906.

(26) J.Burgess. *Ions in Solution: Basic Principles of Chemical Interactions*, 2nd ed.; Woodhead publishing, 2011.

(27) Tanaka, H.; Kawano, M.; Koga, N. Thermogravimetry of Basic Copper(II) Sulphates Obtained by Titrating NaOH Solution with CuSO4 Solution. *Thermochim. Acta* **1991**, *182*, 281–292.

(28) Dirkse, T. P.; Wiers, B. The Stability and Solubility of AgO in Alkaline Solutions. *J.*

Electrochem. Soc. **1959**, *106*, 284.

(29) Lesnykh, N. N.; Tutukina, N. M.; Marshakov, I. K. The Effect of Sulfate and Nitrate Ions on the Passivation and Activation of Silver in Alkaline Solutions. *Prot. Met.* **2008**, *44*, 437–442.

(30) Yagi, S. Potential-PH Diagrams for Oxidation-State Control of Nanoparticles Synthesized via Chemical Reduction. In *Thermodynamics - Physical Chemistry of Aqueous Systems*; Moreno-Piraján, J. C., Ed.; InTech: Rijeka, 2011.

(31) Amlie, R. F.; Rüetschi, P. Solubility and Stability of Silver Oxides in Alkaline Electrolytes. *J. Electrochem. Soc.* **1961**, *108*, 813.

(32) Wang, F.; Eylem, C.; Nanjundaswamy, K.; Iltchev, N. Determination of $AgCuO_2$ Discharge Mechanism in Alkaline Electrolyte. *Electrochem. Solid-State Lett.* **2004**, *7*, A346.

(33) Grendal, O.; Blichfeld, A.; Skjærvø, S.; van Beek, W.; Selbach, S.; Grande, T.; Einarsrud, M.-A. Facile Low Temperature Hydrothermal Synthesis of $BaTiO_3$ Nanoparticles Studied by In Situ X-Ray Diffraction. *Crystals* **2018**, *8*, 253.

(34) Philippot, G.; Jensen, K. M. Ø.; Christensen, M.; Elissalde, C.; Maglione, M.; Iversen, B. B.; Aymonier, C. Coupling in Situ Synchrotron Radiation with Ex Situ Spectroscopy Characterizations to Study the Formation of $Ba_{1-x}Sr_xTiO_3$ Nanoparticles in Supercritical Fluids. *J. Supercrit. Fluids* **2014**, *87*, 111–117.

(35) O'Sullivan, K.; Chiarotti, G.; Madden, P. A. Silver-Ion Disorder in -AgI: A Computer Simulation Study. *Phys. Rev. B* **1991**, *43*, 13536–13548.

(36) Starink, M. J. Kinetic Equations for Diffusion-Controlled Precipitation Reactions. *J. Mater. Sci.* **1997**, *32*, 4061–4070.

(37) Peterson, K. M.; Heaney, P. J.; Post, J. E. A Kinetic Analysis of the Transformation from Akaganeite to Hematite : An in Situ Time-Resolved X-Ray Diffraction Study. *Chem. Geol.* **2016**, *444*, 27–36.

(38) Weinberg, M. C.; Birnie, D. P.; Shneidman, V. A. Crystallization Kinetics and the JMAK Equation. *J. Non. Cryst. Solids* **1997**, *219*, 89–99.

(39) M, F. A.; M, T. The Johnson-Mehl-Avrami-Kolmogorov Model: A Brief Review. *NUOVO Cim.* **1990**, *64*, 305–312.

(40) Starink, M. J.; A.M.Zahra. An Analysis Method for Nucleation and Growth Controlled Reactions at Constant Heating Rate. *Thermochim. Acta* **1997**, *292*, 159–168.

(41) Lu, H.; Wright, D. S.; Pike, S. D. The Use of Mixed-Metal Single Source Precursors for the Synthesis of Complex Metal Oxides. *Chem. Commun***. 2020**, *56*, 854-871.

(42) Zhang, Q.; Liu, S.-J.; Yu, S.-H. Recent Advances in Oriented Attachment Growth and Synthesis of Functional Materials: Concept, Evidence, Mechanism, and Future. *J. Mater. Chem.* **2009**, *19*, 191–207.

(43) Zhang, J.; Huang, F.; Lin, Z. Progress of Nanocrystalline Growth Kinetics Based on Oriented Attachment. *Nanoscale* **2010**, *2*, 18–34.

(44) Inskeep, W. P.; Bloom, R. An Evaluation of Rate Equations for Calcite Precipitation Kinetics at PCO Less than 0 . 01 Atm and PH Greater than 8. *Geochim. Cosmochim. Acta*

1985, *49*, 2165–2180.

(45) G.Koutsoukos, P.; G.Kontoyannis, C. Precipitation of Calcium Carbonate in Aqueous Solutions. *J.Chem.Soc., Fraday Trans* **1984**, *80*, 1181–1192.

For Table of Contents Use Only,

Reaction pathway of the hydrothermal synthesis of $AgCuO_2$ from *in situ* time-resolved X-ray diffraction

*Hongjun Liu[a], Ola G. Grendal[b], Susanne Linn Skjærvø[b,c], Antoine R. M. Dalod[b,d], Wouter van Beek[e], Abderrahime Sekkat[a], Mari-Ann Einarsrud[b], David Muñoz-Rojas[a,]**

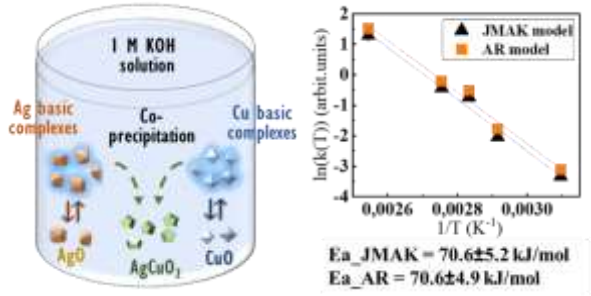

An *in situ* time-resolved XRD study of the hydrothermal formation of $AgCuO_2$ from a suspension of AgO and CuO is presented. The effect of reaction temperature and pH on the reaction kinetics, pathway and the final phases obtained is evaluated. $AgCuO_2$ forms through co-precipitation of basic Ag and Cu copmlexes formed at high pH values. The activation energy of the overall reaction was calculated to be 70.6±5.1 kJ/mol.